fluids

MDPI

Article

Interaction of the Shock Train Leading Edge and Filamentary Plasma in a Supersonic Duct

Loren C. Hahn *, Philip A. Lax, Scott C. Morris and Sergey B. Leonov

Institute for Flow Physics and Control, Aerospace and Mechanical Engineering, University of Notre Dame, Notre Dame, IN 46556, USA; plax@nd.edu (P.A.L.); smorris1@nd.edu (S.C.M.); sleonov@nd.edu (S.B.L.)
* Correspondence: lhahn1@nd.edu

Abstract: Quasi-direct current (Q-DC) filamentary electrical discharges are used to control the shock train in a back-pressured Mach 2 duct flow. The coupled interaction between the plasma filaments and the shock train leading edge (STLE) is studied for a variety of boundary conditions. Electrical parameters associated with the discharge are recorded during actuation, demonstrating a close correlation between the STLE position and dynamics. High-speed self-aligned focusing schlieren (SAFS) and high frame-rate color camera imaging are the primary optical diagnostics used to study the flowfield and plasma morphology. Shock tracking and plasma characterization algorithms are employed to extract time-resolved quantitative data during shock–plasma interactions. Four distinct shock–plasma interaction types are identified and outlined, revealing a strong dependence on the spacing between the uncontrolled STLE and discharge electrodes and a moderate dependence on flow parameters.

Keywords: supersonic; shock train; pseudoshock; plasma; electrical discharge; isolator control; scramjet

check for updates

Citation: Hahn, L.C.; Lax, P.A.; Morris, S.C.; Leonov, S.B. Interaction of the Shock Train Leading Edge and Filamentary Plasma in a Supersonic Duct. *Fluids* **2024**, *9*, 291. https://doi.org/10.3390/fluids9120291

Academic Editors: Robert Martinuzzi, Tatiana Lapushkina and Olga A. Azarova

Received: 8 November 2024
Revised: 23 November 2024
Accepted: 5 December 2024
Published: 7 December 2024

Copyright: © 2024 by the authors. Licensee MDPI, Basel, Switzerland. This article is an open access article distributed under the terms and conditions of the Creative Commons Attribution (CC BY) license (https://creativecommons.org/licenses/by/4.0/).

1. Introduction

Efficient and reliable scramjet operation requires the control of shock-dominated unsteady flows within the isolator [1,2]. Supersonic compression leads to the formation of shock waves with consequent shock–boundary layer interactions (SBLIs) and shock–shock interactions [3]. These interactions are highly sensitive to both upstream and downstream boundary conditions [4–6]. A shock train is a series of compression and expansion waves that are generated in a supersonic duct-driven flow for reasons including an increase in back pressure and thermal choking. A schlieren image of a shock train in a Mach 2 flow is shown in Figure 1. Changes in upstream conditions, such as Mach number and boundary layer characteristics, as well as changes in downstream conditions from combustion instabilities, result in the rapid repositioning of the shock train. This can lead to sudden performance changes and, if the shock train leading edge (STLE) moves far enough upstream, unstart [7,8]. Active control of the shock structure within the isolator is necessary to widen the margin of engine operation, particularly in off-design conditions.

The pressure distribution along the pseudoshock, a region of increasing pressure that consists of a shock train and a primarily subsonic mixing region, is a function of upstream boundary layer characteristics such as the momentum thickness Reynolds number, Re_θ, the confinement ratio, C_θ, the Mach number, M, and the downstream pressure, P_b [9,10]. A variety of methods have been used to manipulate these parameters in order to control the pseudoshock position and structure. Gas injection and suction [11,12], mechanical valves [13], and vortex generators [14] are typical solutions that have been shown to control the pseudoshock. However, the response time of mechanical actuators can be orders of magnitude greater than the relevant gas-dynamic time scales. Electrical gas discharges, on the other hand, offer rapid response due to their nearly inertia-free action.

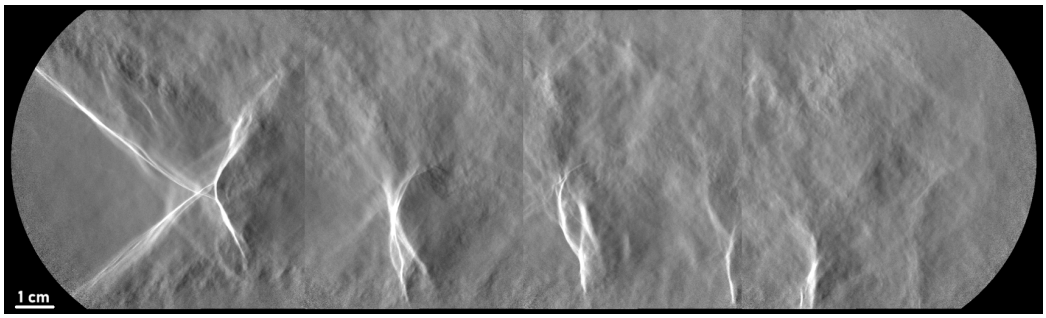

Figure 1. Mach 2 shock train composite image captured during wind tunnel unstart of the SBR-50 facility (flow from left to right).

Quasi-direct current (Q-DC) near-wall filamentary discharges have been used to modify the shock structure in supersonic flows in various configurations. They have been shown to generate shock waves in a manner similar to a soft wedge, with the shock angle increasing with discharge power [15]. They have been used upstream of compression surfaces, resulting in improved total pressure recovery and mass capture [16,17]. More recently, these discharges have been used to position shocks at actuator electrode locations, modifying the global shock structure of the flow path [18–21]. Another feature of Q-DC implementation is the effective transformation of normal shock waves to oblique shock waves, leading to a reduction in total pressure loss [22].

In this work, the shock train structure within a throttled supersonic isolator is modified by three near-wall Q-DC plasma filaments. The dynamics of the STLE and the plasma filaments are studied for a series of flow path conditions that reveal various interaction modes that depend on the uncontrolled STLE position.

2. Experimental Methods

2.1. Flow Path

In this work, the experiments were conducted in the SBR-50 supersonic blowdown wind tunnel facility at the University of Notre Dame. Tests were run at Mach 2 with stagnation quantities of T_0 = 300–490 K and P_0 = 1.6–2.6 bar. The steady-state run time was approximately 500 ms for all tests in this study. The test section has a rectangular cross-section with dimensions 76.2 × 76.2 mm just downstream of the nozzle and a 1° half-angle expansion of the top and bottom walls to compensate for boundary layer growth. A diffuser section begins 704 mm downstream of the nozzle exit, which has adjustable wedge faces on the top and bottom walls. The wedge angle can be set in order to establish the back pressure, P_b, which is taken as the static pressure at the most downstream pressure tap before the diffuser section. Control of the wedge angle enabled the STLE position to be varied from run to run. A schematic of the test section is provided in Figure 2a. The plasma is generated using a Q-DC electrical discharge from three high-voltage electrodes, stabilized by two streamwise-running grounded copper rails, as shown in Figure 2b. The flush-mounted metal components are embedded in a ceramic insert. The electrodes are equally spaced from each other and the sidewalls and the two rails run parallel in the streamwise direction in the middle spaces of the three electrodes. The electrodes are 3.18 mm in diameter, and the grounded rails are 44.5 mm long with a width of 3.18 mm. An initial breakdown occurs between an electrode and a grounded rail, and the plasma filament is lengthened as the ionized gas advects downstream until finally being anchored to the metal wall downstream of the insert. A custom power supply was used to generate the plasma in this work. Electrical probes and an oscilloscope were used to record time series data of gap voltages corresponding to each filament and the current through one of the side filaments during testing. The power supply operated in a current-stabilized mode of I ≈ 5 A with plasma power of roughly W_{pl} = 2.0 kW per filament during stable operation at P_0 = 1.6 bar.

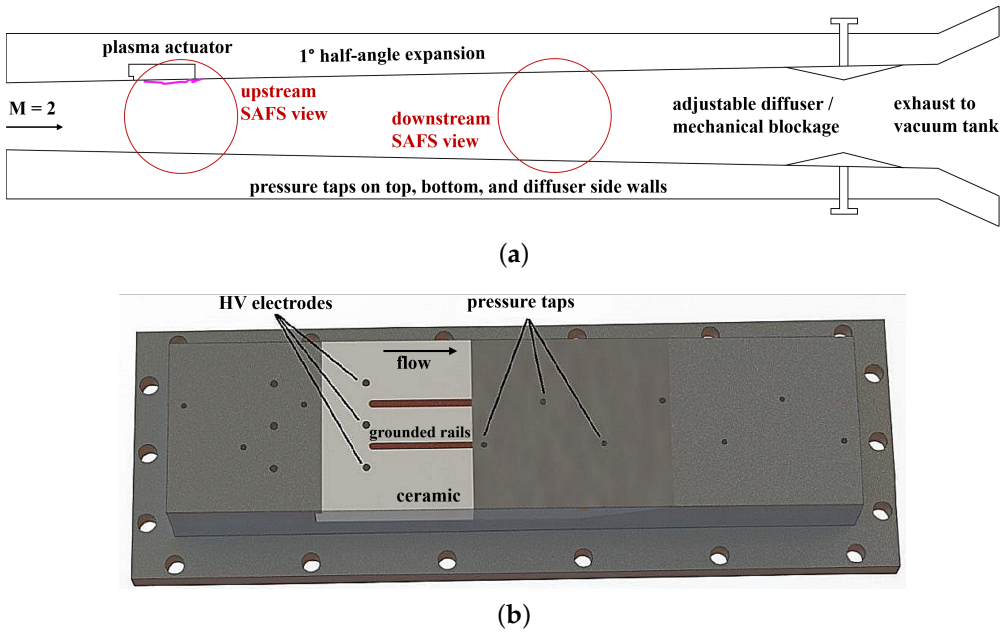

Figure 2. SBR-50 experimental reference images showing (**a**) test section schematic overview and (**b**) top wall plasma actuator insert geometry [20].

2.2. Instrumentation

Pressure taps between the nozzle exit and the diffuser section were spaced 25.4 mm apart in the streamwise direction and staggered about the flowpath center plane on the top and bottom walls, as show in Figure 2b. An additional five pressure taps were spaced 25.4 mm apart on side wall of the diffuser at the height of the center plane. Pressure measurements were acquired at 800 Hz using a 64-channel Scanivalve MPS4264 pressure scanner. Two streamwise quartz window sections covered the extent of the test section upstream of the diffuser to provide optical access for schlieren imaging and high-speed plasma imaging. A self-aligned focusing schlieren system (SAFS) with two field lenses [23] was used for flow visualization. The SAFS images were recorded with a high-speed camera (Phantom v2512, USA) which operated at a frame rate of 20 kHz with an exposure time of 260 ns. The SAFS images were acquired at two different streamwise locations depending on the experimental run, as indicated in Figure 2a. Plasma was imaged using a high-speed color camera (Photron Nova S9 FastCam, USA) which operated at a frame rate of 40 kHz with an exposure time of 2 µs. The color camera was pointed at the plasma through the side windows of the test section. The angle at which the plasma images were recorded varied depending on the view of the SAFS system because the diagnostics were rearranged in the test cell. The change in view was taken into account during image processing.

The plasma and SAFS images were well-synchronized for each experimental case. The first instance of plasma breakdown is visible in the SAFS images and accompanied by a blast wave similar to that of a laser spark [23]. The frames in the plasma and SAFS images that contained the initial breakdown were taken as t_{plasma}.

2.3. Test Parameters

Eight experimental cases are considered. Table 1 presents the cases along with relevant flow path and diagnostic information. Each case was run with a unique angle of the downstream diffuser wedge, resulting in varied static-to-total pressure ratios and shock train lengths. Figure 3 shows the pressure distribution of the uncontrolled flow for each of the cases. The origin of the horizontal axis is set at the streamwise location of the high-voltage electrodes. The physics of the STLE-plasma coupling will be shown to strongly depend on the uncontrolled STLE position.

It is worth noting a few key differences between cases. Case VI was run at an increased stagnation pressure and temperature compared to the other cases. The density, however, was kept constant. Despite its increased diffuser angle, Case VI had a pressure distribution nearly identical to that in Case V, as seen in Figure 3. The differences in the dynamics between Case V and Case VI are assumed to be a direct result of the varied stagnation quantities. Case II had the most downstream STLE of the cases considered. The SAFS system was shifted downstream for this case to the second window of the test section to visualize the STLE during plasma actuation. Figure 2a shows the different SAFS views.

Table 1. Experimental test conditions.

Case	Diff. Angle [°]	$\overline{P}_b/P_0$	Plasma Dur. [ms]	SAFS View	P_0 [bar]	T_0 [K]
I	0	0.104	150	Upstream	1.6	300
II	6.5	0.387	150	Downstream	1.6	300
III	7.5	0.448	100	Upstream	1.6	300
IV	7.75	0.466	100	Upstream	1.6	300
V	8	0.489	100	Upstream	1.6	300
VI	8.25	0.495	100	Upstream	2.6	490
VII	8.5	0.506	100	Upstream	1.6	300
VIII	9	0.535	100	Upstream	1.6	300

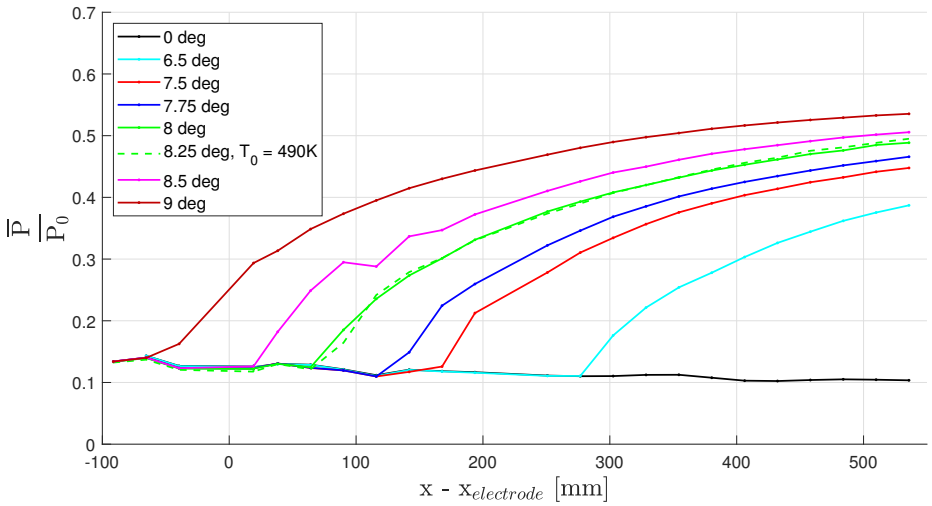

Figure 3. Time-averaged pressure distribution of uncontrolled flow path at various diffuser wedge angles.

3. Data Processing

3.1. Electrical Discharge and Filamentary Plasma Characteristics

Figure 4a provides a wall-normal schematic view of the plasma actuator and the parameters characterizing the discharge pattern. These Q-DC discharge characteristics have been presented in other works [15,20], but will be briefly outlined here for completeness. The middle filament in the schematic illustrates the transient elongation process in five steps. When the voltage difference between the electrode and the grounded rail is sufficiently high, breakdown occurs [24,25]. This begins with a streamer formation between the electrode and the upstream end of the rail, as denoted by marker 1. Because the plasma exists within the gas, the ionized particles advect with the flow in the streamwise direction. The initially short filament stretches in the flow direction while staying anchored to the electrode and rail. Markers 2–4 show the streamwise travel of the elongating plasma. Vorticity effects result in the plasma lifting off the wall [21]. Because the portion of the filament between the electrode and rail lifts out of the boundary layer, the middle portion of the stretching filament moves downstream faster. Finally, the end of the filament reaches the end of the

rail and becomes grounded at the tunnel wall downstream of the ceramic insert, as shown by marker 5.

An undisturbed plasma filament will remain grounded at the wall downstream of the actuator. The top filament in Figure 4a is stable and free of strong disturbances. Some waviness is often observed because the filament exists within a turbulent flow, but these features are minimal. A plasma filament will undergo wrinkling when the flow becomes highly turbulent or separates. Shocks impinging upstream of the actuator have been shown to wrinkle the plasma filaments [20]. If a filament becomes too wrinkled, it may extinguish, and a re-breakdown event near the electrode must occur to re-establish the filament.

Figure 4b shows a sample image of plasma filaments in a Mach 2 flow. Here, the outer two filaments are stably anchored at the downstream tunnel wall, while the center filament is in the elongation process. The filament streamwise distance, d_{SW}, is defined as the maximum extent in the streamwise direction covered by a single filament in an image. This parameter is formally defined as follows. A matrix containing the image indices of pixels containing plasma is defined:

$$\mathbf{x}_{pl} := I(x_1, x_2) > I_{th}, \quad \mathbf{x} \in \mathbb{R}^2, \tag{1}$$

where $\mathbf{x}$ is the full two-dimensional space within the image frame, $I(x_1, x_2)$ is the pixel intensity at pixel location $[x_1, x_2]$, and I_{th} is an intensity threshold for differentiating whether or not a pixel contains plasma. The streamwise distance is then calculated as follows:

$$d_{sw} = \max(\mathbf{x}_1) - \min(\mathbf{x}_1), \tag{2}$$

where x_1 is the streamwise coordinate direction. In Figure 4b, it is clear that a filament can have a varied length for a constant d_{SW}, depending on the wrinkling of the filament. Because the voltage per unit length of a filament is nearly constant, the simultaneous voltage and d_{SW} of a filament give insight into the degree of wrinkling. Additionally, boundary layer separation near the plasma filaments may prevent them from grounding at the downstream tunnel wall. d_{SW} is a useful parameter for monitoring the plasma morphology when it is altered by the flowfield.

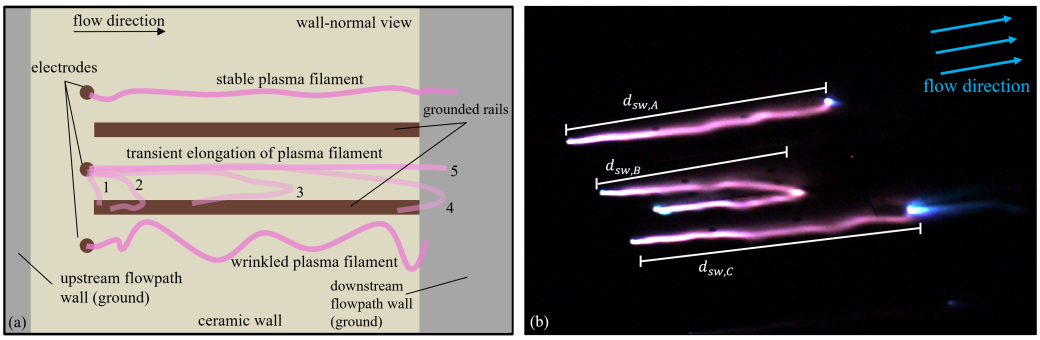

Figure 4. Plasma background: (**a**) schematic describing plasma geometry and elongation process and (**b**) streamwise distance parameter example.

3.2. SAFS Shock Tracking

The shock structures in the flow were tracked so that quantitative data could be extracted from the SAFS images. The shock tracking method in this work accounts for an evolving STLE with variable pixel intensity by finding the most upstream portion of the shock along the line. This is accomplished by setting a threshold value based on the background pixel intensity and finding the most upstream pixel that exceeds this threshold. Figure 5 provides examples of the method used to track the shocks. The row of pixels used for tracking was chosen on a case-by-case basis depending on the observed behavior of the STLE.

Aside from Case II, all cases had SAFS views at the upstream location, as seen in Figure 5a. This view contains the plasma on the top wall, which is known to generate a weak oblique shock in a steady flow [18,20,26]. The shock tracking method was applied to a horizontal row of pixels that was chosen such that the shock could be tracked for the entire duration of the plasma control. Cases I, III-VII tracked where the plasma shock (which would become merged with the STLE) intersected a horizontal line 22 mm above the tunnel centerline. This specific line location is denoted in Figure 5a. The STLE pushed upstream of the electrodes in Case VIII, so the horizontal line was shifted to 11 mm above the centerline and tracked the second shock in the train. The STLE in Case II stayed further downstream than in the other cases. Because the STLE did not interact strongly with the plasma shock, it tended to be less definitive during plasma actuation. For this reason, the normal shock portion of the STLE was tracked. The horizontal line for Case II was placed 14 mm below the centerline because the normal shock was always present at that height, as seen in Figure 5b. It is apparent in this view that the normal shock is not always distinct due to unsteadiness and flow three-dimensionality. The tracking algorithm was monitored, and it was visually determined that the normal shock was reliably detected within 2 mm of accuracy.

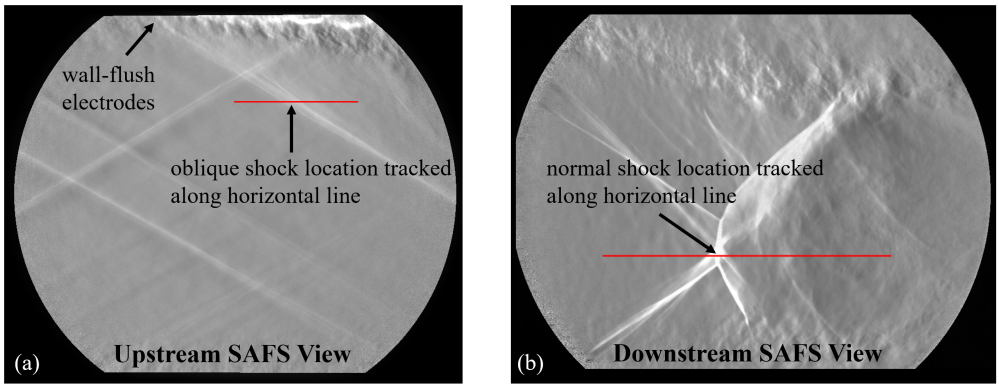

Figure 5. SAFS shock tracking examples showing (**a**) oblique shock tracking for the upstream SAFS view and (**b**) normal shock tracking for the downstream SAFS view.

4. Results

4.1. Electrical Discharge in Absence of Shock Train

Case I was run as a baseline for the plasma actuation with no shock train present. The diffuser wedge angle was set to 0°, resulting in an underexpanded flow where the static pressure continually decreased with streamwise distance due to the diverging tunnel walls. The pressure profile for this case prior to plasma actuation is shown in Figure 3. Figure 6 shows an SAFS image 5 ms prior to plasma actuation, an SAFS image 10 ms after the start of the plasma actuation, and a color plasma image 10 ms after the start of the plasma actuation. Before plasma actuation, the only distinguishable features in the flow path are the top and bottom wall boundary layers and weak Mach waves generated by tunnel geometry such as wall inserts. At Mach 2, a Mach wave is 30° [3] via

$$\sin \mu = \frac{1}{M}. \tag{3}$$

Figure 6b shows the flow field during stable plasma actuation. Light emitted from the plasma filaments, as well as the plasma shock, are visible here. The angle of the shock in this image is 31°. This minute difference from the Mach wave angle highlights the minimal disturbance generated from the plasma in the baseline case. Figure 6c shows three elongated, stable plasma filaments. As noted earlier, the filaments show some degree of waviness, even in the most stable case. This is due to an interaction with a self-consistent pair of vortices generated on both sides of each plasma filament [21].

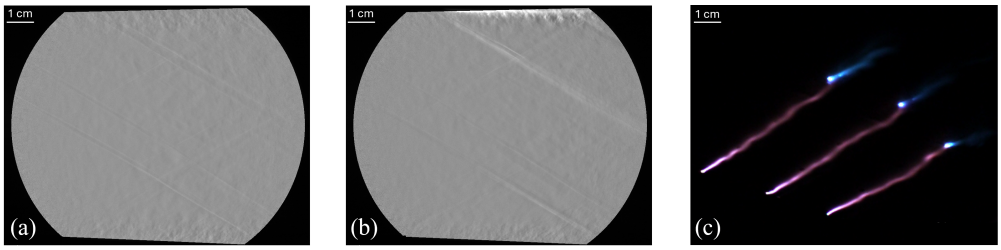

Figure 6. Case I plasma actuation: (**a**) SAFS image at $t - t_{\text{plasma}} = -5$ ms, (**b**) SAFS image at $t - t_{\text{plasma}} = 10$ ms, and (**c**) color plasma image at $t - t_{\text{plasma}} = 10$ ms.

Figure 7 contains time series oscilloscope data (top plot) and the calculated d_{SW} time series (bottom plot) for a single-side filament. The streamwise distance of the plasma is seen to increase relatively slowly from 50 mm to 70–80 mm before rapidly returning to 50 mm. The rail length on the actuator is 44.5 mm. This informs us that the plasma is anchored to the downstream tunnel wall throughout the entire duration of actuation, stretches until reaching its maximum sustainable length, and undergoes re-breakdown to the downstream edge of the ceramic insert and tunnel wall. There were 11 re-breakdown events over the 150 ms plasma duration, yielding an average re-breakdown frequency of about 70 Hz. However, the rate of re-breakdown was somewhat stochastic as the time between events varied between 5–22 ms.

For stable plasma filaments, d_{SW} is nearly equal to the true length of the filament. Keeping this in mind, note that the voltage appears to scale directly with d_{SW} in Figure 7. The current, on the other hand, acts inversely to d_{SW}. It was mentioned above that the power supply operates in a current-stabilized mode. While the current is shown to decrease with plasma length, its standard deviation was only 7% of its mean value. The voltage standard deviation was 12.7% of its mean. The relative magnitude of the voltage change is reflected in the power scaling with voltage and, thus, filament length.

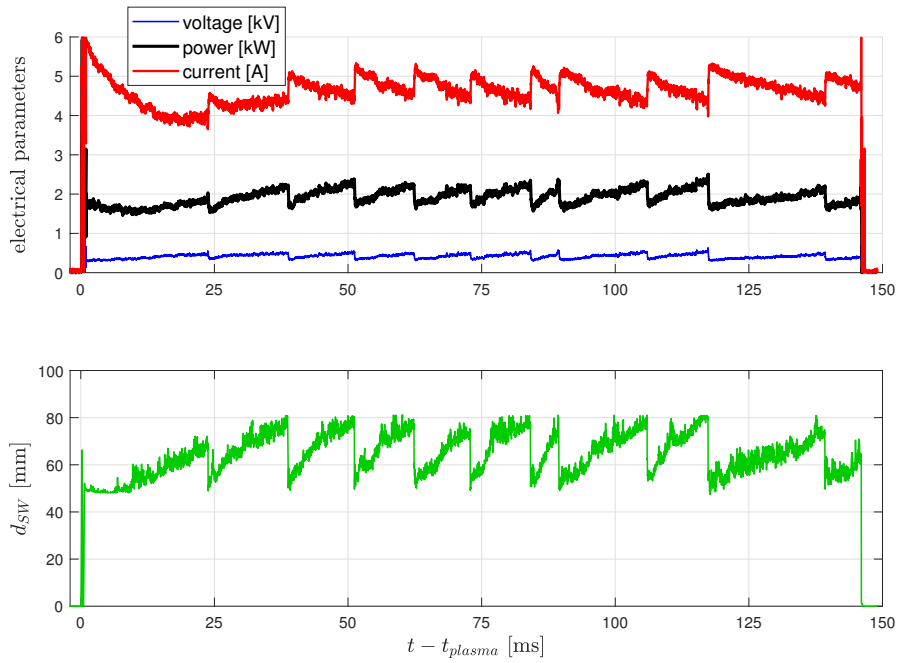

Figure 7. Voltage, power, current (**top**), and streamwise filament distance d_{SW} (**bottom**) of a single plasma filament through time for Case I.

The joint probability distributions of multiple variables are visualized in Figure 8 through the plotting of bivariate histograms. The bivariate histograms group the data into two-dimensional bins and calculate the probability distribution throughout the space based on the number of realizations in each bin. For all bivariate histograms presented in this work, 200 equal-width bins were used in each dimension and covered the exact bounds shown on the plot axes. Figure 8a shows the joint probability distribution of the voltage and power for a single-side filament in Case I. Figure 8b shows the joint probability distribution of d_{SW} and power for a single-side filament in Case I. The inner 75% of the data was used for each of these time series in order to remove the plasma activation and deactivation events. Inspecting Figure 8a, the highest probability marks lie on a diagonal line. This indicates that voltage and power are positively correlated. There are some faint diagonal regions shifted down and right from the main diagonal. This shows that there are a small percentage of instances where the voltage is higher than typical for a given power. These points occurred during the second elongation process of the filament. Looking back at Figure 7, it takes nearly two cycles, or 40 ms, for the current to reach its average value. This transient period may be a result of the actuator components heating up from their "cold" state. Aside from the transient stage, the plasma power scales linearly with the voltage on a single line.

The joint probability distribution of d_{SW} and power is shown in Figure 8b. A linearly increasing region is evident here, but it contains more scatter than the voltage–power distribution. This is likely a result of the plasma waviness that can occur during stable actuation. It should also be noted that the bottom left and top right of the region contain the highest-probability pockets. During an elongation cycle, the filament spends the most time at its shortest and longest streamwise distance.

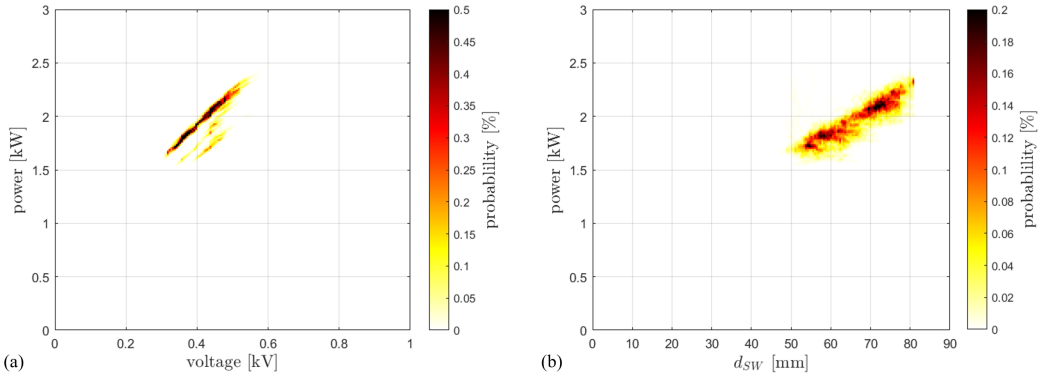

Figure 8. Joint probability distributions for a single plasma filament for Case I: (**a**) power and voltage and (**b**) power and filament streamwise distance.

The streamwise distance of all three filaments during plasma actuation is plotted in Figure 9. All three filaments have the cyclical elongation-to-re-breakdown characteristic. The duration of the cycles and their frequency is of the same order of magnitude between each filament. However, it is clear that the filaments are not synchronized with each other; their re-breakdown events occur independently. This is logical, as the flow is predominantly in the streamwise direction. The ions are largely frozen to the flow since the ion drift velocity is significantly lower than the flow velocity, and the electrons follow the electric field configuration. Therefore, the ionized gases associated with each filament do not mix significantly in this stable case.

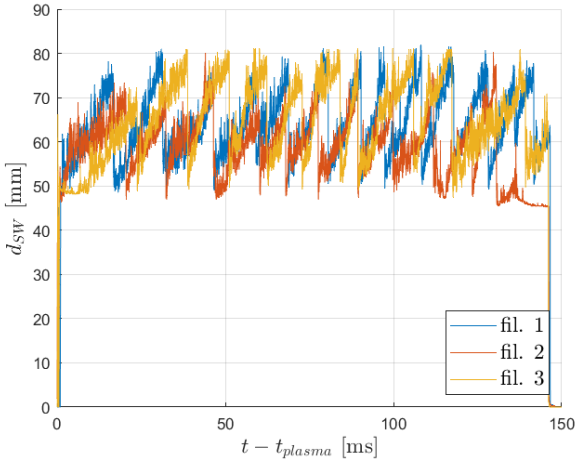

Figure 9. Streamwise distance of each plasma filament through time for Case I.

4.2. Case IV: Intermittent Interaction

Case IV had a flow pressure ratio $\overline{P}_b/P_0$ of 0.466 prior to plasma control, which produced a symmetric shock train with its leading edge roughly 120 mm downstream of the electrodes. During plasma actuation, intermittent upstream propagations of the STLE were observed. These events were observed to strongly disrupt the boundary layer near the plasma actuator. The modified boundary layer flow had a wrinkling effect on the plasma filaments. Figure 10 shows key attributes observed during the intermittent interaction.

Figure 10a plots the SAFS intensity along a horizontal row of pixels (22 mm above the flow path centerline) through time. The black curve shows where the oblique shock intersected this row of pixels. Plots of a similar nature are presented throughout the remainder of this paper. At 0 ms, the actuator is turned on. Almost immediately, a weak plasma shock originating at the electrodes is generated. Figure 10b shows an SAFS image and a corresponding plasma image at 2 ms. The plasma shock and filament shapes are qualitatively similar to those shown in Figure 6. Around 7 ms, the intensity of the pixels downstream of the tracked shock increases. This indicates a density gradient over a significant distance due to compression waves. Figure 10c shows images at 11.4 ms. The SAFS image shows a leading shock with a slightly increased angle and a thickened boundary layer. The shock appears more diffuse and band-like. Although the SAFS system has focusing capabilities, the defocus blur increases linearly with distance from the schlieren object plane and out-of-plane density gradients can sometimes be visible depending on the distance from the object plane. The "smoothness" of the shock, in this instance, is thought to be a result of a gradual compression and/or a three-dimensional shock front. The extinguished center filament, in this instance, confirms at least the latter. The intact side filaments at 11.4 ms are significantly wrinkled as the STLE merges with the plasma shock.

At 29.05 ms, the shock reached its most upstream location along the horizontal line of approximately $x - x_{\text{electrode}} = 20$ mm. Collected images at this timestamp are shown in Figure 10d. Notice that the bottom leg of the STLE has entered the frame. The STLE is now clearly asymmetric and its normal portion has almost been removed entirely. The oblique shock angle increases again from the last instance. All three filaments are intact at 29.05 ms. They are each significantly wrinkled and anchored midway on the copper rails. The reverse flow region that is known to exist under the STLE [4,5] is thought to be preventing the filaments from elongating and anchoring at the tunnel wall downstream of the actuator. By 30.4 ms, the STLE begins to move back downstream. This instance is shown in Figure 10e, where three-dimensionality and plasma extinction are evident again. For the remainder of the 100 ms plasma actuation, the STLE does not propagate more upstream than $x - x_{\text{electrode}} = 27$ mm. The considerable difference between the most and second-most upstream STLE position is a defining characteristic of the intermittent interaction observed in Case IV.

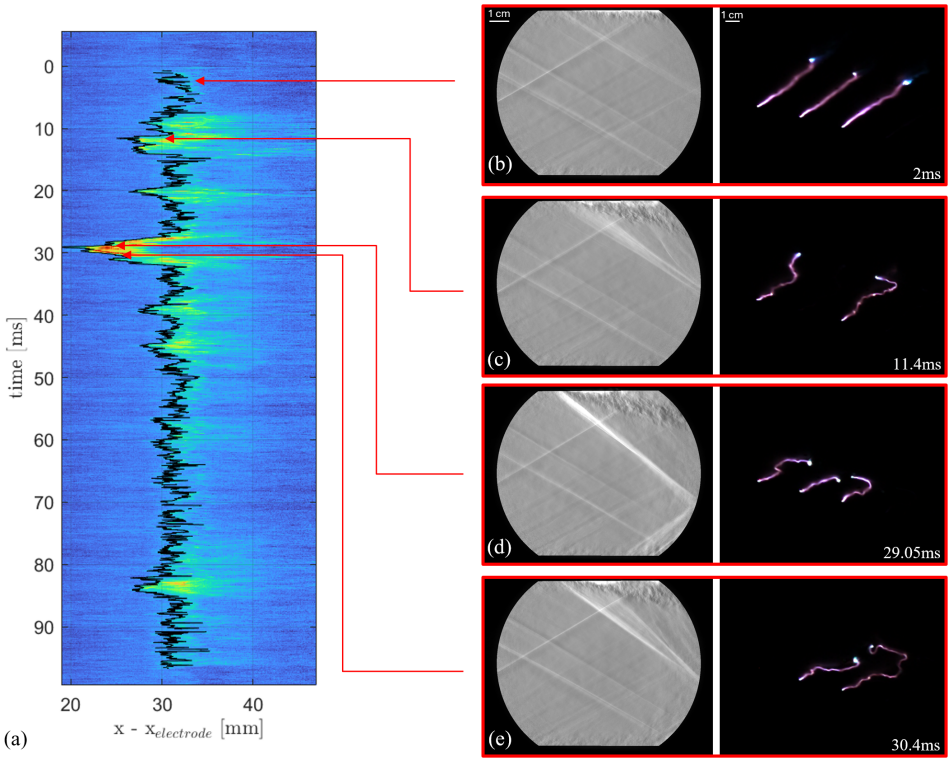

Figure 10. Intermittent shock-plasma interaction for Case IV: (**a**) SAFS pixel intensity along a horizontal line (22 mm above the tunnel centerline) with the tracked shock intersection location shown in black; (**b**–**e**) instantaneous synchronized SAFS and plasma images obtained at denoted timestamps.

Figure 11 shows each of the plasma filament streamwise distances over time. It was shown earlier that all three filaments undergo cycles of elongation and re-breakdown to the end of the edge of the actuator in a steady flow. In Case IV, the outer filaments begin the process of elongation, while the middle filament is relatively fixed in length. When the STLE moves upstream at ∼7 ms, the anchor location of all three filaments moves upstream. By 10 ms, all three filaments begin to sporadically drop to $d_{SW} = 0$ mm. This happens when a filament extinguishes entirely. These extinguishing events occurred when the STLE pushed upstream, increased the pressure in the vicinity of the electrodes, and strongly disturbed the plasma flow.

It is noticeable that there were more filament extinction events between 10–15 ms than there were between 27–32 ms, despite the STLE being its furthest upstream at 29.05 ms. It appears that there was a considerable duration of time in which all three filaments were anchored at ∼30 mm while remaining intact between 27–30 ms. This observation is in agreement with the 29.05 ms plasma image presented in Figure 10d. It was concluded in the discussion in Figure 7 that the discharge power scales with filament length. It could be speculated that the STLE reaches its furthest upstream when it wrinkles the plasma filaments without extinguishing them, resulting in a transient of relatively high discharge power. A longer duration of plasma control would likely be needed to confirm this hypothesis and should be considered as the technology progresses.

The time-averaged pressure distribution along the top wall with and without control for Case IV is provided in Figure 12. The electrical discharge control allows the pressure rise imposed by the downstream blockage to propagate further upstream on the top wall, reaching the electrodes. The pressure gradient is significantly reduced with control, resulting in a lower static pressure near the diffuser section. This is attributed to a reduction in the normal shock portion of the STLE. It is clear that electrical discharge control has a strong effect on the entire flow path. However, modification of the entire pseudoshock is still under investigation, particularly in the unsteady sense. Because the STLE–plasma coupling physics are so rich, the authors have chosen to focus this work on the upstream

interaction, leaving the study of the full pressure field to future work. For this reason, the pressure distributions for the remaining cases will not be explored in this paper.

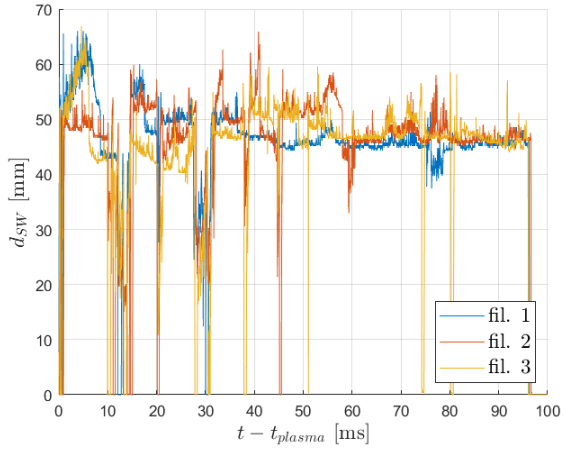

Figure 11. Streamwise distance of each plasma filament through time for Case IV.

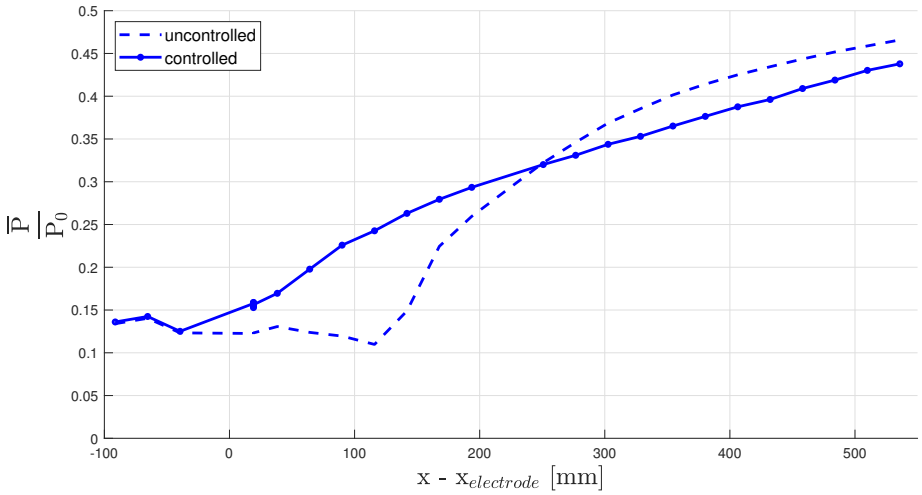

Figure 12. Time-averaged top wall pressure distribution of the uncontrolled and controlled flow path of Case IV.

4.3. Case V: Unsteady Interaction

Case V had a flow pressure ratio $\overline{P}_b/P_0$ of 0.489 prior to plasma control. These boundary conditions yielded a shock train with its leading edge roughly 70 mm downstream of the electrodes. The nearing of the STLE to the plasma actuator resulted in unsteady oscillations of the STLE and wrinkling of the filaments during control. Figure 13a is a plot of the SAFS pixel intensity along a horizontal row of pixels and the tracked shock position through time. The tracked shock curve shows larger amplitude oscillations than those observed in Case IV. These oscillations were unsteady over the entire duration of plasma actuation, aside from a short transient time at initialization.

Figure 13b shows weak plasma shock and elongated filaments at 2 ms. The leftmost filament in the image shows some wrinkling near its downstream ground location. This may indicate that the boundary layer is already being disrupted locally. In this case, it takes about 5 ms for the flow field changes from the STLE to appear in the SAFS images. By 6.5 ms, the top oblique shock of the STLE has merged with the plasma shock, as seen in Figure 13c. The STLE continues to move upstream, and its angle increases. Figure 13d,e shows an STLE that is asymmetric with a reduced normal shock portion moving upstream. The plasma filaments in these instances are disrupted and unable to elongate. The images

in Figure 13e occur at 15.4 ms, which is when the STLE was furthest upstream for this case. The SAFS image still shows an asymmetric STLE with a reduced normal portion. The plasma filaments, however, have anchored to the tunnel wall upstream of the ceramic actuator insert. It appears that the filaments have advected upstream with the reverse flow associated with the STLE.

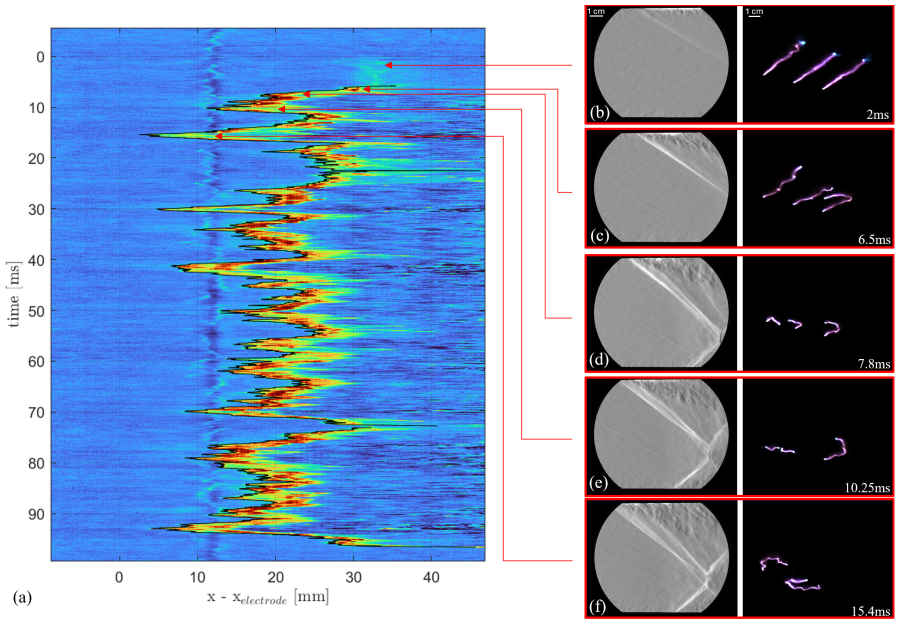

Figure 13. Unsteady shock–plasma interaction for Case V: (**a**) SAFS pixel intensity along a horizontal line (22 mm above the tunnel centerline) with the tracked shock intersection location shown in black; (**b**–**f**) instantaneous synchronized SAFS and plasma images obtained at denoted timestamps.

The streamwise distance of the plasma filaments during actuation for Case V is plotted in Figure 14. The plasma filaments do not elongate once they are grounded on the downstream wall. The d_{SW} of all three filaments appears to decrease slightly over the first 5 ms and then rapidly decrease and/or extinguish entirely as the filaments are disturbed. All of the plasma filaments are extinguished regularly throughout actuation. In fact, there were only a few instances where the filaments were able to elongate along the entire rail length. These instances occurred near 22 ms, 72 ms, and 96 ms. As expected, these times corresponded to the STLE being far downstream in Figure 13a.

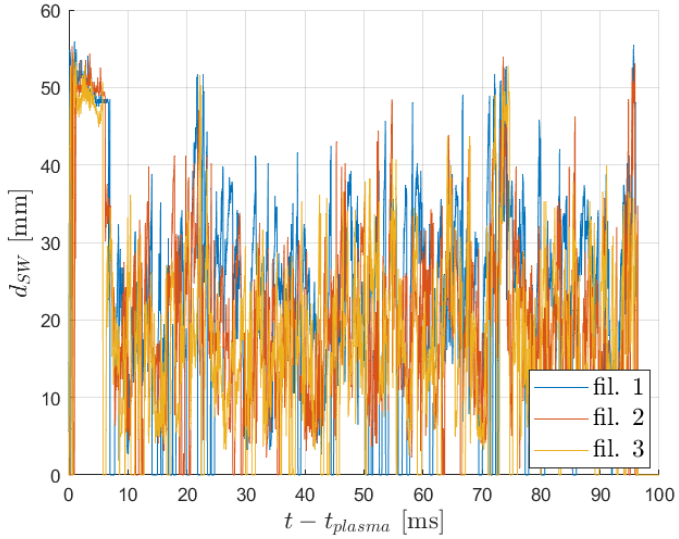

Figure 14. Streamwise distance of each plasma filament through time for Case V.

4.4. Case VIII: Separation Bubble Interaction

The flow pressure ratio $\overline{P}_b / P_0$ was increased further to 0.535 in Case VIII, establishing the STLE upstream of the electrodes by 50 mm. Figure 15b shows the STLE prior to plasma actuation. The electrodes lie between the legs of the top lambda shock of the STLE. During actuation, the STLE moved upstream and out of the SAFS frame. For this reason, the horizontal row of pixels used for shock tracking was set at 11 mm above the tunnel centerline and only covered the downstream half of the SAFS view. This enabled the second shock in the train to be tracked rather than the leading shock.

Figure 15a shows the intensity along the pixel row with the tracked second shock location plotted in black. Density gradients along the pixel row are evident before actuation because the shock train is already present. It takes just over 10 ms for the shock train to move upstream enough for the second shock to be tracked. Figure 15c shows the STLE and plasma filaments just as the shock train starts to move upstream. The top boundary layer is thickened here. However, the STLE structure is not significantly modified like it had been when it began downstream of the electrodes. The plasma filaments at 10 ms are stretched in the upstream direction. It appears that the leftmost filaments in the image are grounded at the rail, while the right filament is grounded upstream of the actuator. At 14 ms, the STLE has continued to make its way upstream without significant structure changes. The filaments are highly disturbed in this instance. The leftmost filament is extinguished, while the rightmost filament has a spiraled shape with its grounding location unclear. At 45 ms, the second shock reaches its most upstream location. Figure 15e now has the STLE entirely out of view. The filaments at this time are all grounded on a rail and unstretched. One particularly interesting quality of this case was the long transient adjustment of the shock train location. In the prior cases, the STLE reached a quasi-steady location in less than 10 ms. In this case, on the other hand, the bulk motion of the shock system is upstream for the first 40 ms. It is supposed that because the actuator sat between the legs of the STLE, reverse flows and stagnant air zones could have prevented the high enthalpy gas from convecting downstream and mixing thoroughly, resulting in a delayed response from the shock train.

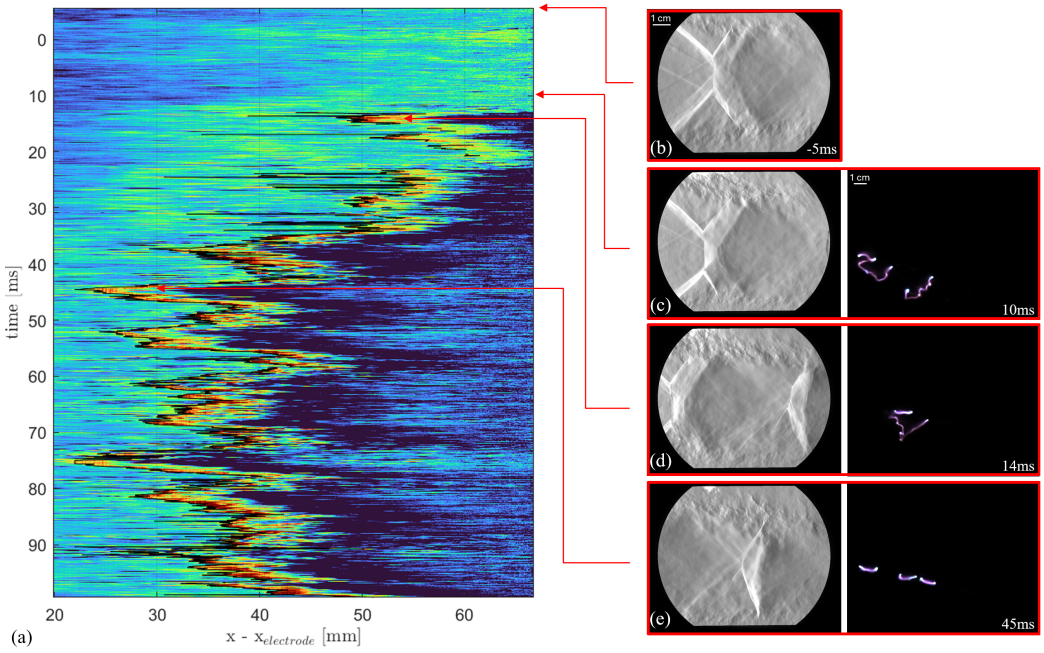

Figure 15. Separation bubble shock–plasma interaction for Case VIII: (**a**) SAFS pixel intensity along a horizontal line (11 mm above the tunnel centerline) with the tracked shock intersection location shown in black; (**b**–**e**) instantaneous synchronized SAFS and plasma images obtained at denoted timestamps.

The filament's streamwise distance for Case VIII is plotted in Figure 16. At the start of plasma actuation, filaments 2 and 3 have an increasing d_{SW}, while filament 1 does not elongate past 10 mm. It should be noted that d_{SW} does not differentiate between a filament distance upstream versus downstream. The value simply quantifies the absolute extent of the filament. While not shown, all three of the filaments were only observed to elongate in the upstream direction here. Throughout this run, the filaments were highly wrinkled and extinguished regularly. A noticeable difference between the separation bubble interaction and the previous interaction types is the filament asymmetry. It is clear in Figure 16 that filament 1 was consistently shorter than the other filaments by about 20 mm. This may indicate three-dimensionality within the shock train boundary layer.

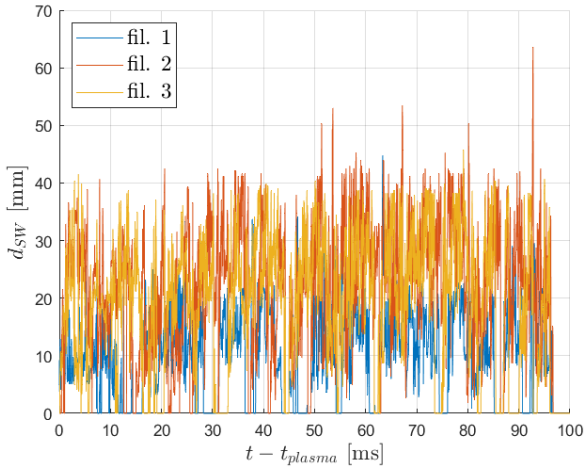

Figure 16. Streamwise distance of each plasma filament through time for Case VIII.

4.5. Case II: Isolated Interaction

The interaction types discussed thus far focused on scenarios where the STLE was close enough to the plasma actuator that a coupled interaction occurred. The STLE structure was modified by the plasma control and brought upstream, causing the filaments to become disturbed to varying degrees. In Case II, a tunnel pressure ratio of $\overline{P}_b/P_0 = 0.387$ generated a shock train with its leading edge 280 mm downstream of the electrodes. The STLE was sufficiently far enough downstream to isolate the plasma from the boundary layer thickening and reverse flows associated with the shock train. Because the STLE existed far downstream, a second SAFS view location was required during control, and the normal shock portion of the STLE was tracked. The intensity along a SAFS pixel row and the tracked normal shock location are plotted in Figure 17a. It is seen that the shock location begins to move upstream almost immediately when the control begins. Relatively large amplitude oscillations occur over the duration of the plasma control.

Instantaneous SAFS and plasma images are highlighted in the figure as well. Figure 17b shows a symmetric STLE with a significant normal portion prior to control. Figure 17c–e shows a similar modification of the STLE structure as was observed when the shock was near the plasma. The top oblique leg moves upstream and decreases in angle, while the bottom leg geometry is relatively unchanged. The normal shock size is decreased significantly. Because the STLE was too far downstream to merge with the plasma shock, the top leg is less distinct. Figure 17d shows images from the instant the STLE was furthest upstream. Here, the top leg of the STLE is nearly indistinguishable. It seems that the pressure rise that occurs through the shock train is happening more gradually as the shock moves upstream, resulting in a near-isentropic compression through the top half of the STLE. The plasma images included in Figure 17 show stable plasma filaments that elongate and re-breakdown independently. The plasma behavior is qualitatively similar to the STLE-free Case I. A quantitative assessment of the plasma statistics will be considered in the following section.

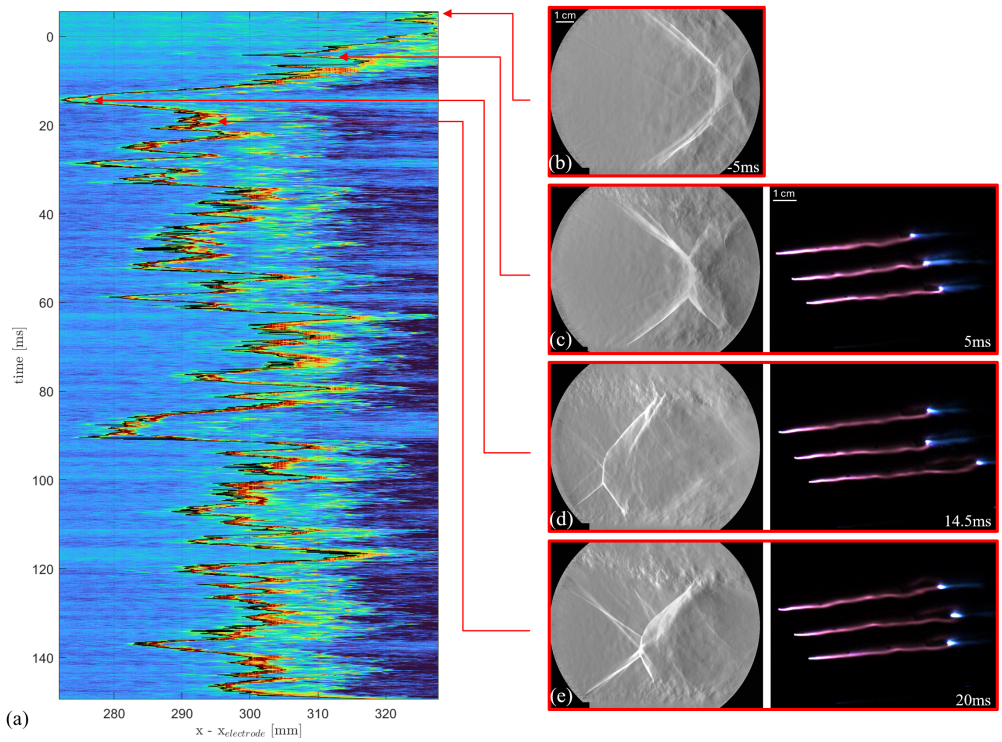

Figure 17. Indirect shock–plasma interaction for Case II: (**a**) SAFS pixel intensity along a horizontal line (14 mm below the tunnel centerline) with the tracked shock intersection location shown in black; (**b**–**e**) instantaneous synchronized SAFS and plasma images obtained at denoted timestamps.

5. Discussion

Four STLE–plasma interaction types have been identified: intermittent interaction, unsteady interaction, separation bubble interaction, and isolated interaction. The interaction type experienced by the flowfield is largely determined by the distance between the STLE and the discharge electrodes prior to control. The interaction type for each case is provided in Table 2, with the uncontrolled STLE distance from the electrodes included. Figure 18 contains plots of the tracked shock location and average streamwise distance of the three plasma filaments for cases that were run with the upstream SAFS view. The interaction type differences are apparent in these plots. Before this plot is discussed, however, it is reiterated that the shock is tracked using the view of the SAFS images. For cases with intermittent and isolated interactions, the STLE may be oscillating downstream of the SAFS view; therefore, this plot is not necessarily representative of the STLE oscillation amplitude at all times. The curves capture the movement of the plasma shock, which may become merged with the STLE as it propagates upstream. Case II and Case VIII are omitted from this figure because the tracking algorithm in those cases differed from the others. In the figure, $x_{uncontrolled}$ is defined as the streamwise location where a Mach wave (30°) originating from the electrodes would intersect the tracking pixel row.

Table 2. Interaction types by case.

Case	$\frac{x_{STLE}-x_{elec}}{h}$	Interaction Type
I	N/A	N/A
II	3.7	Isolated
III	2.2	Isolated
IV	1.7	Intermittent
V	1.0	Unsteady
VI	1.0	Intermittent
VII	0.25	Unsteady
VIII	−0.7	Separation Bubble

The shock curves for Cases I and III in Figure 18 are indistinguishable. Their $\overline{d}_{SW}$ curves are similar, with Case III exhibiting more irregularity in its filament elongation process. While not included in the figure, it was noted earlier that the $\overline{d}_{SW}$ behavior in Case II was similar to that of Case I. The $\overline{d}_{SW}$ curve of Case III indicates some subtle affect on the electrical discharges by pressure waves in the boundary layer associated with the STLE; however, it was not significant enough to extinguish any filament. For this reason, Case III is considered an isolated interaction. Case IV, discussed in detail earlier, is an intermittent interaction. This is clear in both plots of Figure 18, as the shock position and filament distances move together, deviating from and returning to their initial states at irregular intervals. Cases V and VII both have characteristics of an unsteady interaction. Following a short transient period at the beginning of actuation, their STLEs merge with the plasma shock for the remainder of the run. They exhibit unsteady, large amplitude STLE oscillations for the entirety of plasma control. For Case V, the filament distances were drastically reduced as the STLE traveled upstream and never returned to a stable state for the remainder of the run.

Case VI was included in Figure 18 because it highlights the effect of increased flow pressure and temperature (with fixed density). The uncontrolled pressure distribution in Case VI was nearly identical to that of Case V. However, the increased flow temperature yielded a different interaction during electrical discharge. The STLE was not positioned as far upstream as it was in the "cold" flow. It also did not directly interact with the plasma filaments throughout the entire run. This is evident in the $\overline{d}_{SW}$ time series, as the filament distances were regularly elongating to the end of the copper rails (~50 mm) between instances of strong disturbance. Case VI is considered an intermittent interaction for these reasons. Because the energy deposition to the flow by the electrical discharges is nearly constant across all the cases, an increase in flow temperature decreases the ratio of the discharge energy to the flow enthalpy. Considering this, it makes sense that the control authority would be reduced from Case V to Case VI.

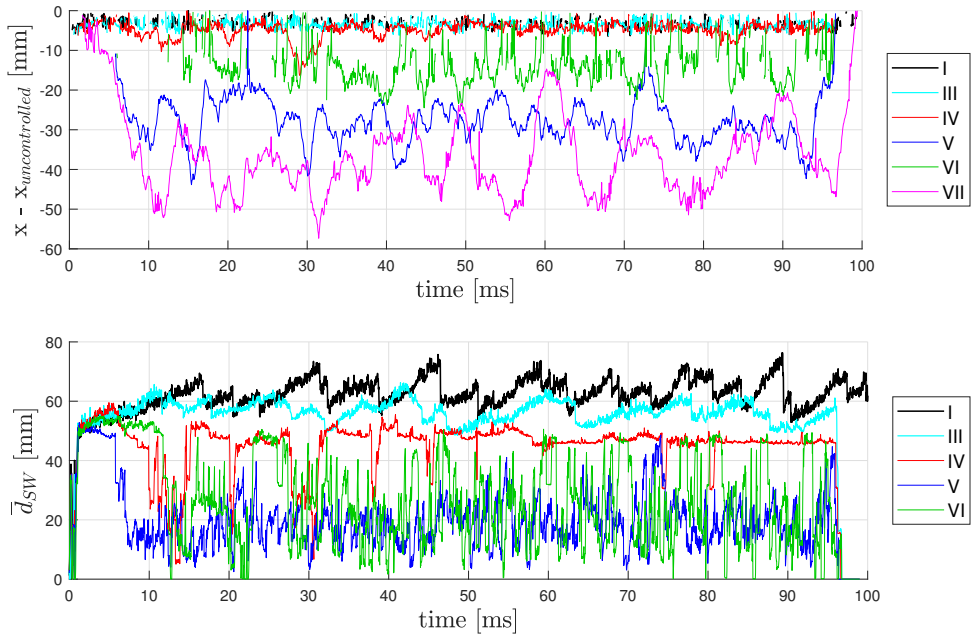

Figure 18. Time series data for selected upstream SAFS view cases during plasma actuation: Shock location (**top**) and average of streamwise distance of all three filaments through time (**bottom**).

Figure 19 presents the time-average value and standard deviation of a single filament d_{SW} for a selection of cases. The middle 75% of the controlled flow data was used for these statistics to isolate the quasi-steady portion of the electrical discharges. It is clear that for the cases with the STLE absent or far downstream, d_{SW} was longest on average with a

fairly small standard deviation, resulting from the elongation-re-breakdown process. Case III, while being considered an isolated interaction, shows a moderately reduced average d_{SW}. Mentioned in the discussion in Figure 18, there is likely some subtle interaction occurring that is preventing the filaments from elongating fully. Case IV has a further decreased average streamwise distance with an increase in standard deviation due to its intermittency. Case V shows a minimum in d_{SW}, resulting from the strong interaction between the filaments and the STLE. The standard deviation is slightly smaller than in Case IV but is quite large relative to the average. The qualities of Case VI reinforce the notion of it being an intermittent interaction. The average d_{SW} is larger than in Case V, highlighting the lessened effect on the filaments by the STLE. Most noteworthy, though, is the standard deviation. It is clear that the filament distance varied greatly throughout the run, transitioning between fully elongated filaments and shortened, highly wrinkled filaments. Finally, the separation bubble interaction of Case VIII showed similar statistics to the unstable interaction of Case V. Both of these interaction types were associated with a perpetually disturbed filament region.

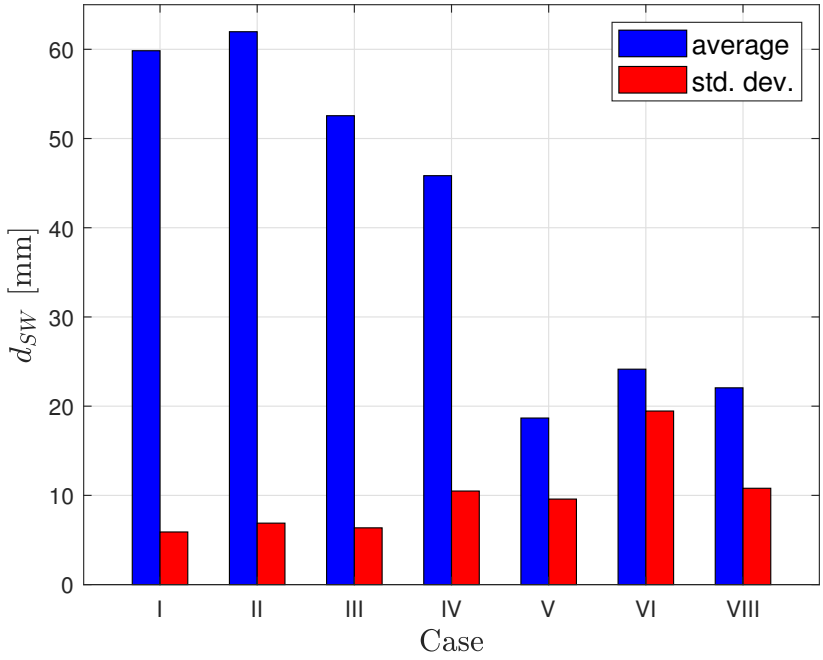

Figure 19. Streamwise plasma filament distance statistics.

Joint probability distributions of d_{SW} and power are provided for a selection of cases in Figure 20. The methods for generating these plots are the same as those described in Figure 8. Cases I and II are shown in Figure 20a,b and are notably similar to each other. It appears that there are four pockets of the highest probability for Case II as opposed to the two pockets mentioned previously for Case I. This indicates that the plasma filament tended to "pause" at a few preferred lengths throughout the run. The cause of this is not well understood but can be assumed to be a result of the far downstream, but present, shock train. Case III in Figure 20c still exhibits a grouping that is positively correlated, but it is more dispersed than the previous cases. The grouping is also shortened and shifted upward compared to the previous cases. This shows that the d_{SW} varies over a smaller range, and the power tends to be higher for a given d_{SW}. This shows that the filaments are becoming wrinkled in this case.

The bottom row of cases in Figure 20 shows stronger interactions with the plasma filaments. The highest probability region in Figure 20d (Case IV) is a straight vertical line at $d_{SW} = 47$ mm. This distance corresponds to the filament being anchored right at the downstream tunnel wall. There is scatter on all sides about this line and a low probability

cloud that tails in a curve to the left, initially increasing in power and then decreasing in power. This sparse, curved shape is also visible in Figure 20e (Case VI). Considering the power scales with filament length for a given d_{SW}, these sparse trails highlight occurrences with significant wrinkling/stretching. See [20,2.75] in Figure 20e, for example. There is a considerable probability that the power is near its stable value for a d_{SW} of half its stable value. Case VIII, shown in Figure 20f, has a large region of nearly constant probability. The lack of correlation between power and d_{SW} is a noteworthy feature of the separation bubble interaction.

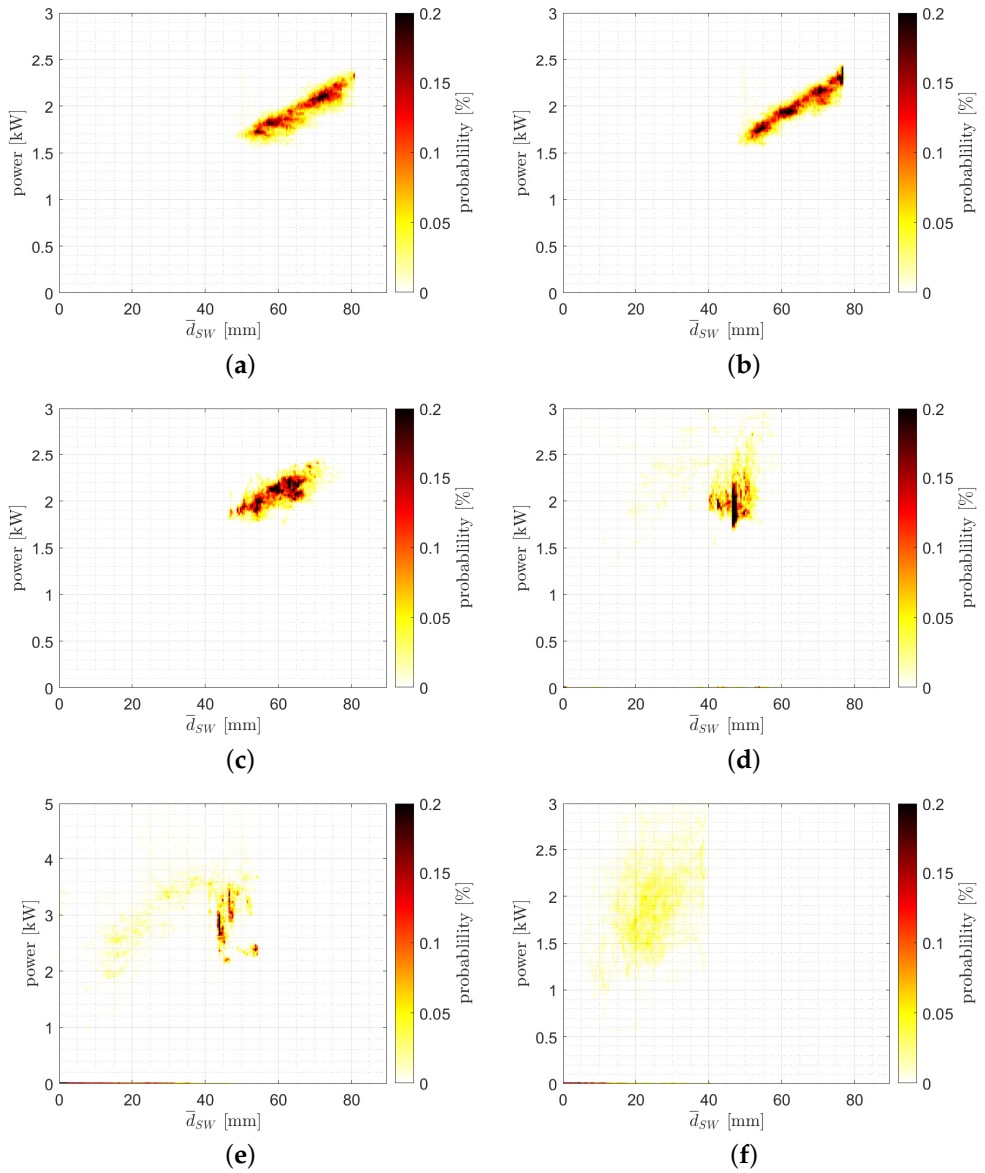

Figure 20. Joint probability distributions of power and filament streamwise distance for a single plasma filament: (**a**) case I, (**b**) case II, (**c**) case III, (**d**) case IV, (**e**) case VI, and (**f**) case VIII.

Various types of STLE–plasma interactions have been identified, and their characteristics have been quantified. While certain details of these processes vary between cases, a general overview of the interaction characteristics is provided in Figure 21. The mechanism of interaction is considered as follows:

(a) Prior to control, a symmetric STLE is located downstream of the electrodes. Strong boundary layer thickening/separation exists underneath the legs of the STLE as a result of the strong adverse pressure gradient imposed downstream.

(b) Once the electrical discharges are initiated, a weak plasma shock is generated from the volumetric expansion of the hot gas in the boundary layer. A short transient period in the range of a few ms occurs before the STLE is noticeably modified.

(c) High-temperature regions in the boundary layer originating from the electrical discharge locally increase the speed of sound. This introduces additional subsonic passages to the electrodes, which enables the downstream pressure to rise to push upstream. The boundary layer displacement thickness associated with the STLE leg moves upstream as the top leg is spread into a series of compression waves. The previously symmetric STLE is now biased upstream on the top leg, which has a reduced angle compared to the initial lambda shock. The shock–shock interaction (Edney Type II [27]) is weakened, resulting in a reduction of the normal shock size. When the STLE is in the vicinity of the electrodes, the plasma filament begins to become wrinkled at this stage.

(d) As the STLE continues to move upstream, it completely merges with the plasma shock. The thickened boundary layer reaches the electrode position and strongly disturbs the filaments. The flow may be reversed in this region and can result in the plasma filaments anchoring upstream of the electrodes. When this happens, the oblique shock becomes anchored even further upstream.

(e) The STLE position was observed to oscillate for all interaction types. The unsteadiness is believed to be a result of the communication lag throughout the shock train as the pressure gradient is modified transiently by the plasma control. Once the STLE travels some distance upstream, it tends to return downstream at fairly large amplitudes (1 duct height). Additionally, as the STLE reaches far upstream, the filaments begin to extinguish regularly. This can reduce the control authority and further contribute to the unsteadiness.

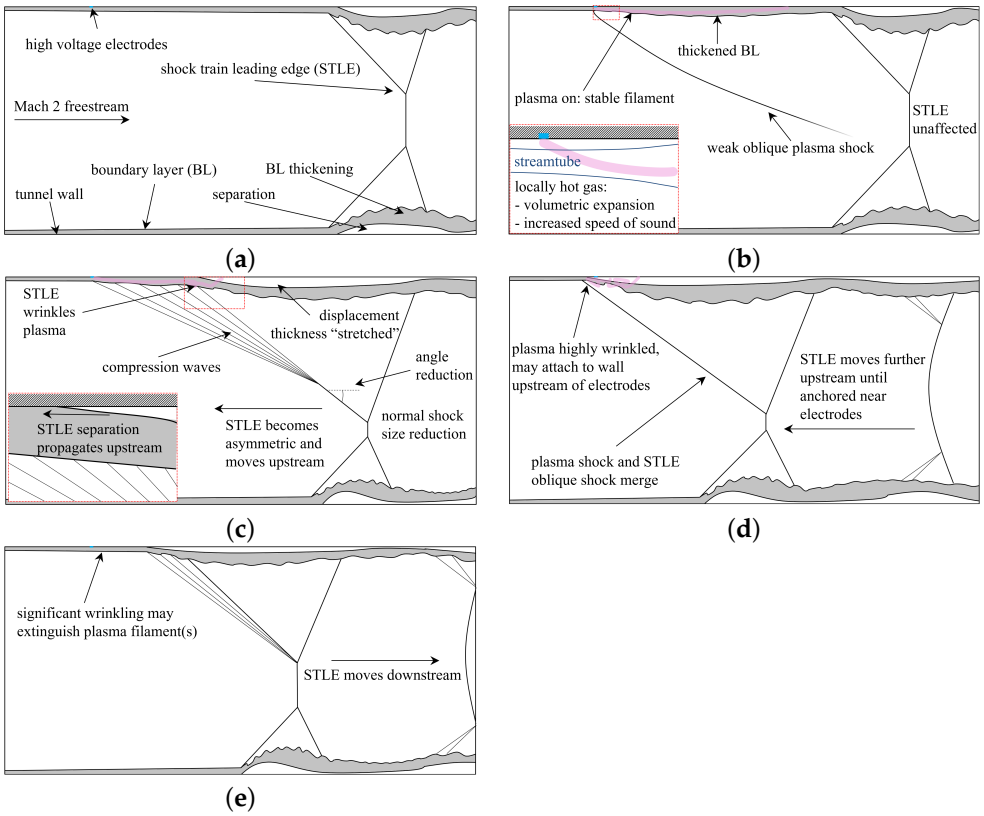

Figure 21. STLE–plasma interaction schematic diagram: (**a**) uncontrolled STLE, (**b**) electrical discharge initiation, (**c**) STLE transition and upstream movement, (**d**) plasma shock and STLE leg merge far upstream, and (**e**) plasma filaments extinguish.

6. Conclusions

An experimental study was performed in order to characterize the interaction of Q-DC filamentary electrical discharges and the shock train in a back-pressured Mach 2 duct-driven flow. A self-aligned focusing schlieren system with a sampling rate of 20 kHz and a color camera with a sampling rate of 40 kHz were used to capture the transient shock and filamentary plasma physics during the interaction. Electrode gap voltage measurements were simultaneously acquired with high-voltage probes, providing data on the electrical discharge dynamics and statistics. Previous work had been conducted on the control of shock wave position and reflection patterns with electrical discharges, but this study expands on the current understanding through the deliberate control of the downstream boundary conditions that establish the shock train. Post-processing techniques, including shock tracking and plasma image measurements, were utilized, allowing time-resolved quantitative data to be extracted from the optical diagnostics.

Four distinct interaction types were identified, and their patterns were described. Isolated interactions occurred when the uncontrolled STLE was placed sufficiently far downstream of the discharge electrodes. The flow pressure field and STLE structure are modified by the electrical discharge control in this interaction, but the plasma filaments remain stable. Isolated interactions occurred when the uncontrolled STLE was over 2.2 duct heights downstream of the electrodes. Intermittent interactions exhibit stable, elongated filaments that are intermittently wrinkled and potentially extinguished as the STLE moves upstream and is anchored to the electrodes. Intermittent interaction occurred when the uncontrolled STLE was ∼1.7 duct heights downstream of the electrodes. Unsteady interactions exhibit an oscillating STLE structure that is constantly wrinkling/extinguishing the plasma filaments. This interaction was observed when the uncontrolled STLE was 0.25–1 duct heights downstream of the electrodes. Separation bubble interactions occurred when the uncontrolled STLE was upstream of the electrodes. This interaction had a relatively long transient evolution of the STLE position, and strong reverse flows that anchored the plasma filaments upstream of the electrodes. Finally, it was observed that increasing the tunnel T_0 weakened the interaction. Specifically, an increase in T_0 from 300 K to 490 K changed the interaction type from unsteady to intermittent for the same uncontrolled STLE position.

Control of supersonic internal flows by electrical discharges has important practical benefits. The reduction in the normal shock portion of the STLE has been shown to reduce total pressure losses and static pressure recovery for a fixed downstream blockage. The ability to rapidly modify the flow field in the compression section of a high-speed air-breathing engine might feasibly expand the operability range of a vehicle. This study of shock–plasma interaction physics sheds light on the potential for applications such as shock positioning and combustion stabilizing in a ramjet or scramjet engine.

Author Contributions: Conceptualization, S.B.L. and L.C.H.; methodology, L.C.H.; formal analysis, L.C.H., S.C.M. and S.B.L.; investigation, L.C.H. and P.A.L.; resources, S.B.L.; data curation, L.C.H.; writing—original draft preparation, L.C.H.; writing—review and editing, S.B.L. and S.C.M.; visualization, P.A.L.; supervision, S.B.L. and S.C.M.; project administration, S.B.L.; funding acquisition, S.B.L. All authors have read and agreed to the published version of the manuscript.

Funding: This work was funded by the US Air Force Office of Scientific Research (PM Dr. Gregg Abate) grant # FA9550-21-1-0006.

Data Availability Statement: The data supporting the conclusions of this article will be made available by the authors upon reasonable demand.

Conflicts of Interest: The authors declare no conflicts of interest.

References

1. Im, S.k.; Do, H. Unstart phenomena induced by flow choking in scramjet inlet-isolators. *Prog. Aerosp. Sci.* **2018**, *97*, 1–21. [CrossRef]

2. Klomparens, R.; Driscoll, J.F.; Gamba, M. Response of a shock train to downstream back pressure forcing. In Proceedings of the 54th AIAA Aerospace Sciences Meeting, San Diego, CA, USA, 4–8 January 2016. [CrossRef]
3. Anderson, J.D. *Modern Compressible Flow: With Historical Perspective*, 3rd ed.; McGraw-Hill Series in Aeronautical and Aerospace Engineering; McGraw-Hill: Boston, MA, USA, 2003.
4. Matsuo, K.; Miyazato, Y.; Kim, H.D. Shock train and pseudo-shock phenomena in internal gas flows. *Prog. Aerosp. Sci.* **1999**, *35*, 33–100. [CrossRef]
5. Gnani, F.; Zare-Behtash, H.; Kontis, K. Pseudo-shock waves and their interactions in high-speed intakes. *Prog. Aerosp. Sci.* **2016**, *82*, 36–56. [CrossRef]
6. Babinsky, H.; Harvey, J. (Eds.) *Shock Wave-Boundary-Layer Interactions*; Cambridge Aerospace Series; Cambridge University Press: Cambridge, UK; New York, NY, USA, 2011; OCLC: ocn701672464.
7. Baccarella, D.; Liu, Q.; McGann, B.; Lee, G.; Lee, T. Isolator-combustor interactions in a circular model scramjet with thermal and non-thermal choking-induced unstart. *J. Fluid Mech.* **2021**, *917*, A38. [CrossRef]
8. Wagner, J.L.; Yuceil, K.B.; Valdivia, A.; Clemens, N.T.; Dolling, D.S. Experimental Investigation of Unstart in an Inlet/Isolator Model in Mach 5 Flow. *AIAA J.* **2009**, *47*, 1528–1542. [CrossRef]
9. Waltrup, P.J.; Billig, F.S. Structure of Shock Waves in Cylindrical Ducts. *AIAA J.* **1973**, *11*, 1404–1408. [CrossRef]
10. Hunt, R.; Edelman, L.M.; Gamba, M. Scaling of pseudoshock length and pressure rise. In Proceedings of the 2018 AIAA Aerospace Sciences Meeting, Kissimmee, FL, USA, 8–12 January 2018. [CrossRef]
11. Do, H.; Im, S.; Godfrey Mungal, M.; Cappelli, M.A. The influence of boundary layers on supersonic inlet flow unstart induced by mass injection. *Exp. Fluids* **2011**, *51*, 679–691. [CrossRef]
12. Weiss, A.; Olivier, H. Shock boundary layer interaction under the influence of a normal suction slot. *Shock Waves* **2014**, *24*, 11–19. [CrossRef]
13. Hunt, R.; Driscoll, J.F.; Gamba, M. Periodic forcing of a shock train in Mach 2.0 flow. In Proceedings of the 55th AIAA Aerospace Sciences Meeting, Grapevine, TX, USA, 9–13 January 2017. [CrossRef]
14. Valdivia, A.; Yuceil, K.B.; Wagner, J.L.; Clemens, N.T.; Dolling, D.S. Control of Supersonic Inlet-Isolator Unstart Using Active and Passive Vortex Generators. *AIAA J.* **2014**, *52*, 1207–1218. [CrossRef]
15. Leonov, S.B.; Yarantsev, D.A. Control of separation phenomena in a high-speed flow by means of the surface electric discharge. *Fluid Dyn.* **2008**, *43*, 945–953. [CrossRef]
16. Falempin, F.; Firsov, A.A.; Yarantsev, D.A.; Goldfeld, M.A.; Timofeev, K.; Leonov, S.B. Plasma control of shock wave configuration in off-design mode of M = 2 inlet. *Exp. Fluids* **2015**, *56*, 54. [CrossRef]
17. Watanabe, Y.; Elliott, S.; Firsov, A.; Houpt, A.; Leonov, S. Rapid control of force/momentum on a model ramp by quasi-DC plasma. *J. Phys. D Appl. Phys.* **2019**, *52*, 444003. [CrossRef]
18. Houpt, A.; Hedlund, B.; Leonov, S.; Ombrello, T.; Carter, C. Quasi-DC electrical discharge characterization in a supersonic flow. *Exp. Fluids* **2017**, *58*, 25. [CrossRef]
19. Houpt, A.; Leonov, S.; Ombrello, T.; Carter, C.; Leiweke, R.J. Flow Control in Supersonic-Cavity-Based Airflow by Quasi-Direct-Current Electric Discharge. *AIAA J.* **2019**, *57*, 2881–2891. [CrossRef]
20. Elliott, S.; Lax, P.; Leonov, S.B. Control of Shock Positions in a Supersonic Duct by Plasma Array. In Proceedings of the AIAA SCITECH 2022 Forum, San Diego, CA, USA & Virtual, 3–7 January 2022. [CrossRef]
21. Andrews, P.; Lax, P.; Leonov, S. Triggering Shock Wave Positions by Patterned Energy Deposition. *Energies* **2022**, *15*, 7104. [CrossRef]
22. Leonov, S.B.; Andrews, P.S.; Ombrello, T.; Braun, E. Shock Wave Train Control in Supersonic Duct. In Proceedings of the AIAA SCITECH 2024 Forum, Orlando, FL, USA, 8–12 January 2024. [CrossRef]
23. Lax, P.A.; Leonov, S.B. Application of High-Speed Self-Aligned Focusing Schlieren System for Supersonic Flow Velocimetry. *Aerospace* **2024**, *11*, 603. [CrossRef]
24. Raizer, I.P. *Gas Discharge Physics*; Springer: Berlin/Heidelberg, Germany; New York, NY, USA, 1997.
25. Go, D.B. *Ionization and Ion Transport: A Primer for the Study of Non-Equilibrium, Low-Temperature Gas Discharges and Plasmas*; Morgan & Claypool Publishers: Kentfield, CA, USA, 2018. [CrossRef]
26. Leonov, S.B.; Yarantsev, D.A. Near-Surface Electrical Discharge in Supersonic Airflow: Properties and Flow Control. *J. Propuls. Power* **2008**, *24*, 1168–1181. [CrossRef]
27. Edney, B. *Anomalous Heat Transfer and Pressure Distributions on Blunt Bodies at Hypersonic Speeds in the Presence of an Impinging Shock;* Technical Report FFA-115; Flygtekniska Forsoksanstalten: Stockholm, Sweden, 1968. [CrossRef]

Disclaimer/Publisher's Note: The statements, opinions and data contained in all publications are solely those of the individual author(s) and contributor(s) and not of MDPI and/or the editor(s). MDPI and/or the editor(s) disclaim responsibility for any injury to people or property resulting from any ideas, methods, instructions or products referred to in the content.